

Cite this: *Soft Matter*, 2014, 10, 8267

Lattice-Boltzmann simulations of droplet evaporation

Rodrigo Ledesma-Aguilar,^{†*a} Dominic Vella^a and Julia M. Yeomans^b

We study the utility and validity of lattice-Boltzmann (LB) simulations to explore droplet evaporation driven by a concentration gradient. Using a binary-fluid lattice-Boltzmann algorithm based on Cahn–Hilliard dynamics, we study the evaporation of planar films and 3D sessile droplets from smooth solid surfaces. Our results show that LB simulations accurately reproduce the classical regime of quasi-static dynamics. Beyond this limit, we show that the algorithm can be used to explore regimes where the evaporative and diffusive timescales are not widely separated, and to include the effect of boundaries of prescribed driving concentration. We illustrate the method by considering the evaporation of a droplet from a solid surface that is chemically patterned with hydrophilic and hydrophobic stripes.

Received 16th June 2014
Accepted 15th August 2014

DOI: 10.1039/c4sm01291g

www.rsc.org/softmatter

1 Introduction

Recent advances in fluid manipulation at submillimetre scales have driven a resurgence of interest in evaporation phenomena.¹ When a drop evaporates, the associated loss of mass leads to readjustments in the drop shape which is in turn affected by interactions with any adjacent solid surfaces. For example, on rough rigid surfaces the rim of an evaporating drop tends to pin on the solid leading to a stick-slip dynamics that can affect the evaporation time.² When pinned, large-scale internal flows force the accumulation of suspended particles near the contact line. This so-called coffee-stain effect is a powerful and still developing route to drive the self-assembly of nano-materials.³ If the solid is elastic, the competition between surface-tension and elastic forces can lead to interesting effects.⁴ For instance, evaporating drops have successfully been used to guide the controlled folding of elastic sheets into prescribed structures.⁵ The interplay between evaporation, surface-tension and elasticity can also have undesired outcomes, *e.g.*, in solvent evaporation from micro-engineered elastic surfaces, where surface-tension forces can lead to the stiction and failure of the delicate micro-pattern.^{6,7}

Modelling evaporation involves accounting for the dynamics of both liquid and gas phases, the liquid–gas interface, and the solid–liquid–gas contact line. In general, one needs to account for mass, momentum and energy transport in both phases.

Adding to the complexity of the problem, physical systems involve changes in the surface energy and topography of the solid. The resulting problem is thus challenging from a computational perspective.

One popular computational tool for studying evaporation is molecular dynamics (MD).⁸ The use of MD has led to several new insights into evaporation driven by temperature differences, including the observation that the temperature may be discontinuous across the droplet interface.⁹ However, MD is most useful in situations where the quantity of liquid that is evaporating is relatively small since simulating large ensembles of molecules is costly. This also makes modelling situations that involve significant flow of the evaporating liquid difficult.

Lattice-Boltzmann (LB) simulations have become a standard tool in computational fluid dynamics, offering a number of advantages compared to other methods. When compared with MD, it is a particular advantage that LB is based on a local kinetic algorithm that reproduces the mass and momentum balance equations at large scales. In doing so, LB also circumvents the non-local constraints of other multiphase models, such as boundary integral representations. Several LB multiphase models have been used successfully to study a variety of interfacial phenomena.¹⁰ Recently, LB simulations have proved useful to gain insight in complex geometries, such as the wetting transition on superhydrophobic surfaces,^{11,12} 3D effects in hydrodynamic instabilities,^{13,14} contact-line hysteresis,¹⁵ and entrainment.¹⁶ A particular advantage that an LB treatment of evaporation would bring is the possibility of studying evaporation in the presence of flow and on complex microstructured surfaces.

In this paper we focus on the validation of the LB method as a physical way to model evaporation phenomena. As a proof of principle we present simulations of the evaporation of planar films and sessile droplets, *i.e.*, drops of typical size below the

^aOxford Centre for Collaborative Applied Mathematics, Mathematical Institute, University of Oxford, Radcliffe Observatory Quarter, Woodstock Road, Oxford OX2 6GG, UK

^bRudolf Peierls Centre for Theoretical Physics, University of Oxford, 1 Keble Road, Oxford OX1 3NP, UK

[†] Present address: Department of Physics and Electrical Engineering, Northumbria University Newcastle, Ellison Place, Newcastle upon Tyne NE1 8ST, UK. E-mail: odrigo.ledesma@northumbria.ac.uk

capillary length, from smooth rigid surfaces. In Section 2, we start our discussion with a brief presentation of evaporation in the context of Cahn–Hilliard dynamics and the LB algorithm, where we include the effects of mass and momentum transport in both phases. We focus on isothermal systems, where the evaporation is dominated by concentration gradients. These are included by means of boundary conditions at the edges of the simulation domain. Our approach departs from the recent work of Safari *et al.*,¹⁷ who considered the evaporation of one- and two-dimensional fronts subject to prescribed thermal gradients imposed at the fluid–fluid interface. Section 3 is devoted to simulation results of the evaporation of a planar film, introducing and discussing the relevant physical timescales. We then validate droplet evaporation simulations against analytical predictions in simple 3D geometries in Section 4 before applying the LB algorithm to give qualitative understanding of the evaporation of a droplet from a chemically patterned substrate in Section 5. Finally, in Section 6 we present the conclusions of this work.

2 LB algorithm

In this section we describe the LB algorithm used in our simulations. We start by considering the equilibrium state of the system. The thermodynamics of the liquid and vapour phases is described by the free-energy functional¹⁸

$$\mathcal{F}[\phi(\mathbf{r}), \rho(\mathbf{r})] = \int_{\Omega} d\Omega \left(\mathcal{V}(\phi) + \frac{1}{2} k |\nabla \phi|^2 + \frac{1}{3} \rho \ln \rho \right) + \int_S dS (h \phi_s), \quad (1)$$

where $\phi(\mathbf{r})$ is the phase field and $\rho(\mathbf{r})$ is the fluid density field. The first integral on the RHS of eqn (1) corresponds to the bulk contribution to the free energy and consists of three terms: the ρ -dependent term represents the free-energy density of an ideal gas and is included to help enforce incompressibility. The non-ideal behaviour of the system is contained in the ϕ -dependent terms. First, the mixing free-energy density $\mathcal{V}(\phi)$ determines the phase behaviour of the fluid. Here we choose the familiar Landau model for a binary fluid, $\mathcal{V}(\phi) \equiv \frac{1}{2} a \phi^2 + \frac{1}{4} b \phi^4$, where $a < 0 < b$, allowing the formation of two equilibrium phases that represent the liquid and the vapour. The square-gradient term prevents the stabilisation of arbitrarily small neighbouring domains, inducing instead the formation of a macroscopic interface whose surface energy can be controlled by an appropriate choice of the parameter k . The second integral on the RHS of eqn (1) is a Cahn-type surface free energy that depends on the local surface concentration $\phi_s(\mathbf{r})$, where S is the surface of the solid-fluid interface. By choosing the parameter h this term can be used to model wetting properties, *i.e.*, by introducing a preferential attraction of one of the two phases to the solid surface.

The equilibrium density and concentration fields follow by minimising the free energy; requiring that the first variation of \mathcal{F} vanishes leads to the set of equations

$$\mu \equiv \frac{\delta \mathcal{F}}{\delta \phi} = \frac{d\mathcal{V}}{d\phi} - k \nabla^2 \phi = 0, \quad (2)$$

and

$$\hat{\mathbf{n}} \nabla \phi|_S = -\frac{h}{k}, \quad (3)$$

where $\mu(\phi)$ is the chemical potential of the binary mixture and $\hat{\mathbf{n}}$ is the local normal unit vector pointing into the solid boundary.

Close to the interface, the phase field varies as a hyperbolic tangent with the normal coordinate to the interface, r ,

$$\phi(r) = \phi_{\text{eq}} \tanh \left(\frac{r}{\varepsilon} \right), \quad (4)$$

where $\phi_{\text{eq}} \equiv \sqrt{-a/b}$ sets the bulk concentration values, *i.e.* $\lim_{r \rightarrow \pm \infty} \phi(r) = \pm \phi_{\text{eq}}$, and $\varepsilon \equiv \sqrt{-k/2a}$ is the interface thickness. The pressure tensor is

$$P_{\alpha\beta} = \left[\frac{1}{3} \rho + \phi \frac{d\mathcal{V}}{d\phi} - \mathcal{V} - k \left(\phi \nabla^2 \phi + \frac{1}{2} |\nabla \phi|^2 \right) \right] \delta_{\alpha\beta} + k \partial_{\alpha} \phi \partial_{\beta} \phi, \quad (5)$$

where the ϕ -dependent terms give rise to interfacial forces. Specifically, it can be shown that the pressure drop across the interface obeys the Young–Laplace equation,

$$\Delta P = \gamma \kappa,$$

where $\gamma \equiv \sqrt{-8ka^3/9b^2}$ is the surface tension and κ is the interface curvature. Similarly, the force balance at the solid-liquid-vapour boundary is dictated by Young's equation, which defines the equilibrium contact angle θ_c , *via*

$$\cos \theta_c = \frac{1}{2} \left[- \left(1 - \frac{h}{\sqrt{kb}} \right)^{3/2} + \left(1 + \frac{h}{\sqrt{kb}} \right)^{3/2} \right] \quad (6)$$

In this paper we shall assume that the system is isothermal, which has been shown to be a reasonable approximation for evaporation driven by concentration gradients.¹ The hydrodynamic equations governing the motion of the fluid are therefore the continuity equation,

$$\partial_t \rho + \partial_{\alpha} (\rho v_{\alpha}) = 0, \quad (7)$$

the Navier–Stokes equations,

$$\partial_t (\rho v_{\alpha}) + \partial_{\beta} (\rho v_{\alpha} v_{\beta}) = -\partial_{\beta} P_{\alpha\beta} + \partial_{\beta} \left[\eta \left(\partial_{\beta} v_{\alpha} + \partial_{\alpha} v_{\beta} - \frac{2}{3} \delta_{\alpha\beta} \partial_{\gamma} v_{\gamma} \right) + \xi \delta_{\alpha\beta} \partial_{\gamma} v_{\gamma} \right] \quad (8)$$

and the Cahn–Hilliard convection-diffusion equation,

$$\partial_t \phi + \partial_{\alpha} (\phi v_{\alpha}) = -\partial_{\alpha} j_{\alpha}, \quad (9)$$

where $\mathbf{v}(\mathbf{r})$ is the velocity field, η and ξ are the shear and second viscosities, and summation over repeated Greek indices is implied.

An important feature of the coupled system given by eqn (8) and (9) is their behaviour close to the triple line. For sharp interface approximations, enforcing the no-slip boundary condition along the wall leads to the well-known viscous dissipation singularity at the contact line.¹⁹ This divergence is naturally regularised by the diffuse interface model by virtue of the diffusive term in eqn (9), which allows for diffusive transport along the wall.^{20,21} The key ingredient needed to model evaporation in the Cahn–Hilliard equation is the diffusive flux \mathbf{j} , which obeys the constitutive equation

$$j_\alpha = -M\partial_\alpha\mu. \quad (10)$$

Here M , often called the mobility parameter, plays the role of a diffusivity. In the limit of weak deviations from equilibrium, $\mu \sim \phi$ and eqn (10) reduces to the familiar Fick's law. In general, M can be chosen to differ between the two phases or even to depend on the local concentration field, *e.g.*, to model situations where diffusive transport is limited by one phase, or is coupled to an external field. For our current purpose, which is to examine the validity of the model for studying evaporation under isothermal conditions, we restrict ourselves to the case of constant M throughout both phases.

In order to complete the model equations we need to specify boundary conditions at the solid wall, and away from the fluid–fluid interface. Similarly to eqn (3), which is a Neumann boundary condition for ϕ at the wall defined by the surface S , we impose

$$\hat{\mathbf{n}} \cdot \nabla \rho|_S = 0, \quad (11)$$

along with the impenetrability and no-slip boundary conditions

$$\hat{\mathbf{n}} \cdot \mathbf{v}|_S = 0 \quad (12)$$

and

$$\hat{\mathbf{t}} \cdot \mathbf{v}|_S = 0, \quad (13)$$

with $\hat{\mathbf{t}}$ the unit tangent vector to the wall.

Because of the finite size of the simulation domain, we need to impose further boundary conditions at the simulation domain edges. We use periodic boundary conditions for the velocity and density fields. To drive the evaporation we impose the Dirichlet boundary condition

$$\phi|_{S_H} = \phi_H, \quad (14)$$

where S_H is a surface enclosing the system. Imposing a given value of ϕ on this boundary, eqn (14), is similar to imposing a surface of constant concentration when solving the diffusion equation for the vapour concentration. However, as in the classical diffusion problem, other boundary conditions, such as a fixed flux, can be more suitable for certain situations.

To integrate the set of eqn (7)–(9) we use the LB algorithm described in ref. 22. We discretise the system using a cubic

mesh with lattice spacing $\Delta x = 1$. We consider the discrete time evolution of two sets of velocity distribution functions, f_i and g_i , each associated with a velocity vector \mathbf{c}_i . The time dependence of the distribution functions is given by the LB equations

$$f_i(\mathbf{r} + \mathbf{c}_i\Delta t, t + \Delta t) - f_i(\mathbf{r}, t) = -\frac{\Delta t}{\tau}(f_i - f_i^{\text{eq}}), \quad (15)$$

and

$$g_i(\mathbf{r} + \mathbf{c}_i\Delta t, t + \Delta t) - g_i(\mathbf{r}, t) = -\frac{\Delta t}{\tau_g}(g_i - g_i^{\text{eq}}). \quad (16)$$

The distribution functions undergo a collision step, corresponding to the right-hand side of eqn (15) and (16), where they relax towards the equilibrium values f_i^{eq} and g_i^{eq} . Here we use the BGK collision operator, where the relaxation step occurs over the timescales τ and τ_g , respectively. After the collision step, distribution functions are advected to neighbouring sites in the lattice as indicated by the left-hand side of eqn (15) and (16). We set the time step to $\Delta t = 1$, so the set of velocity vectors $\{\mathbf{c}_i\}$ completely defines the connectivity of the lattice. Here we use the D3Q15 model,²² where each lattice site is connected to its six nearest and eight third-nearest neighbours.

The link between the LB algorithm and the hydrodynamic equations is established by enforcing mass and momentum conservation during collisions and by choosing the equilibrium distribution functions to be consistent with both the form of the stress tensor and the thermodynamic model. The hydrodynamic variables are defined as

$$\rho \equiv \sum_i f_i, \quad \rho v_\alpha \equiv \sum_i c_{i\alpha} f_i, \quad \phi \equiv \sum_i g_i. \quad (17)$$

Mass and momentum conservation are thus enforced by requiring

$$\sum_i f_i^{\text{eq}} = \rho, \quad \sum_i c_{i\alpha} f_i^{\text{eq}} = \rho v_\alpha, \quad \sum_i g_i^{\text{eq}} = \phi, \quad (18)$$

and the higher order moments of the distribution functions are defined as

$$\sum_i f_i^{\text{eq}} c_{i\alpha} c_{i\beta} = P_{\alpha\beta} + \rho v_\alpha v_\beta, \quad (19)$$

and

$$\sum_i g_i^{\text{eq}} c_{i\alpha} c_{i\beta} = \overline{M}\mu\delta_{\alpha\beta} + \phi v_\alpha v_\beta. \quad (20)$$

The equilibrium distribution functions are written as expansions in the velocity, *e.g.*,

$$f_i^{\text{eq}} = \rho\omega_i \left(A_i + 3v_\alpha c_{i\alpha} + \frac{9}{2}v_\alpha v_\beta c_{i\alpha} c_{i\beta} - \frac{3}{2}v^2 + G_{\alpha\beta} c_{i\alpha} c_{i\beta} \right), \quad (21)$$

where the coefficients are fixed by enforcing eqn (19) and by observing the symmetry conditions imposed by the lattice. A similar expression is used for g_i^{eq} . The values of the coefficients are reported in ref. 22 and are omitted here for brevity.

The hydrodynamic equations are recovered by performing a Chapman–Enskog expansion of eqn (15) and (16), and using eqn (17)–(20). The transport coefficients are related to the LB relaxation times by

$$\eta = \frac{2\tau - 1}{6}$$

and

$$M = \frac{\tau_g - 1}{2} \overline{M}.$$

Boundary conditions at solid surfaces are imposed using bounce-back rules,²³ which recover the impenetrability and no-slip boundary conditions approximately half way between solid and fluid lattice sites.

3 Evaporation of a planar film

3.1 Analytical approach

We first consider the evaporation of a planar fluid film from a solid. The liquid is taken as the phase where $\phi > 0$. The interface is oriented parallel to the xy plane and sits initially at $z = z_0$ while the solid wall is located at $z = z_w < z_0$ (see Fig. 1a). To drive the evaporation of the film we impose the boundary condition $\phi(z = z_H, t) = \phi_H$, where $\phi_H < -\phi_{eq}$. This induces a gradient in the chemical potential field $\mu(\phi(z, t))$. In response to this imbalance, the system reduces ϕ , which corresponds to the evaporation of the film.

For small departures from equilibrium we expect that convective effects are negligible. Therefore, eqn (9) simplifies to

$$\frac{\partial \phi}{\partial t} = M \frac{\partial^2 \mu}{\partial z^2}. \quad (22)$$

Furthermore, we assume that the timescale of diffusion of the phase field, τ_D , is much shorter than the evaporation timescale of the film, τ_E . In such a case the volume behaviour of the phase field is expected to be quasi-static, so that $\partial^2 \mu / \partial z^2 = 0$. It follows that in the gas phase ($z > z_i$) the chemical potential profile is

$$\mu(z) = \mu_i + \frac{\mu_H - \mu_i}{z_H - z_i(t)} (z - z_i(t)), \quad (23)$$

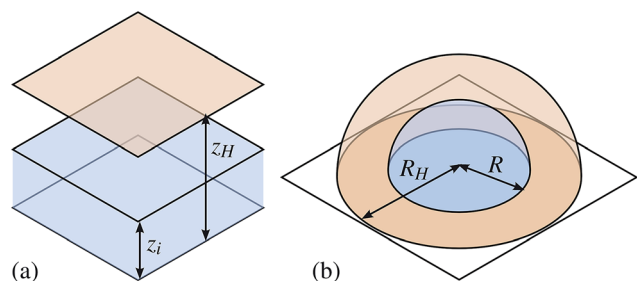


Fig. 1 Schematic representation of the (a) planar film and (b) spherical droplet configurations used in the simulations. The evaporation is driven by setting the phase field out of equilibrium at the orange shaded surfaces.

where $\mu_H \equiv \mu(z_H) \approx \mu(\phi_H)$, $\mu_i \equiv \mu(z_i)$ and z_i is the instantaneous position of the interface. Note that here the boundary condition eqn (14) is translated into a condition for the chemical potential. The chemical-potential gradient at the interface is

$$\left. \frac{d\mu}{dz} \right|_{z_i} = \frac{\mu_H - \mu_i}{z_H - z_i(t)}.$$

Inserting this expression into eqn (10) and using the relation $\dot{z}_i \equiv dz_i/dt \approx j/\Delta\phi$ we find the speed of the interface \dot{z}_i . This can then be integrated with respect to time to find the evolution of the interface height,

$$z_i(t) = z_H - \left((z_H - z_0)^2 - 2 \frac{M(\mu_H - \mu_i)}{\Delta\phi} t \right)^{1/2}. \quad (24)$$

3.2 LB simulations

The simple planar film geometry allows us to test the applicability of the LB algorithm to model evaporation. We performed simulations in a box consisting of $N_x \times N_y \times N_z = 1 \times 1 \times 150$ lattice sites. Periodic boundary conditions were set in the x and y directions. A wall was located at $z_w = 1$, while the concentration was fixed to a value ϕ_H at $z_H = N_z$ to drive the system out of equilibrium. The initial height of the film was set to $z_0 = 100$. Model parameters, in simulation units, are summarised in Table 1. Note that the density and relaxation times in both fluids were set to unity. This minimises the effect of spurious velocities associated with the single-relaxation time LB used here. However, viscosity contrasts can be modelled using multiple-relaxation time algorithms.²⁴

In each simulation the phase and chemical potential fields were tracked, with particular focus on the effect of the phase-field imbalance, defined as $\Delta\phi_H \equiv -\phi_{eq} - \phi_H$. Fig. 2 shows profiles of $\phi(z)$ and $\mu(z)$ for different values of $\Delta\phi_H$ after 5×10^5 simulation steps. As expected, the interface moves towards the wall, *i.e.*, z_i decreases as the liquid evaporates. Furthermore, evaporation proceeds faster for larger $\Delta\phi_H$ or, rather, the amount of liquid lost after a given time has elapsed increases with increasing $\Delta\phi_H$. In all cases, the chemical potential shows an approximately linear profile through the gas phase, which changes to a flat profile in the liquid over a length scale comparable to the interface thickness ε . We observe small deviations from the equilibrium concentration in the liquid phase; the size of these deviations increases with $\Delta\phi_H$. These lead to a small increase of the plateau in the chemical potential with $\Delta\phi_H$, which can be characterised by the value at the interface μ_i as shown in the inset of Fig. 2b.

Since $\Delta\phi_H$ is kept constant throughout the simulations, the interface gradually slows down as evaporation proceeds. We

Table 1 Simulation parameters

ρ	τ	τ_g	a	b	k	M
1	1	1	-0.00305	0.00305	0.0078	5.0

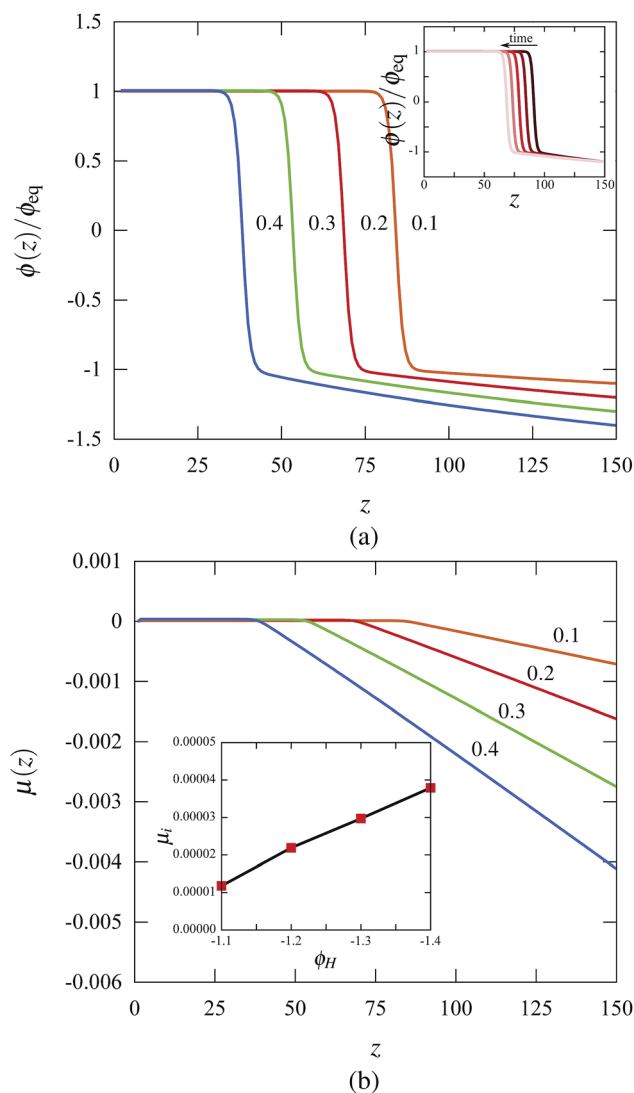


Fig. 2 Phase-field and chemical potential profiles for the planar-film evaporation after 5×10^5 simulations steps. (a) The concentration field is driven out of equilibrium by imposing a prescribed concentration value ϕ_H at the edge of the simulation box ($z = z_H$). The inset shows the time evolution for $\Delta\phi_H/\phi_{eq} = 0.2$ at intervals of 10^5 time steps. (b) The chemical potential shows a linear profile in the gas phase, and remains constant in the liquid, except for small deviations at the interface, which grow with the external driving (inset). The numbers next to each curve correspond to the phase-field imbalance, $\Delta\phi_H$.

recorded both the evaporation speed and the gradient of the chemical potential at the interface at various times during the simulation. As shown in Fig. 3a, the speed of evaporation \dot{z}_i scales linearly with the chemical-potential gradient as expected from eqn (10). A linear fit of the data gives a slope ≈ 2.4 , in close agreement with the expected value $M/\Delta\phi = 2.5$.

The time evolution of the position of the interface is shown in Fig. 3b. We present simulation results along with the analytical prediction, eqn (24), where μ_i is fixed at the value measured in the simulations (Fig. 2b inset) and $\mu_H \approx a\phi_H + b\phi_H^3$. We find good agreement between theory and simulation, with the smallest deviations observed for the smallest $\Delta\phi_H$ values.

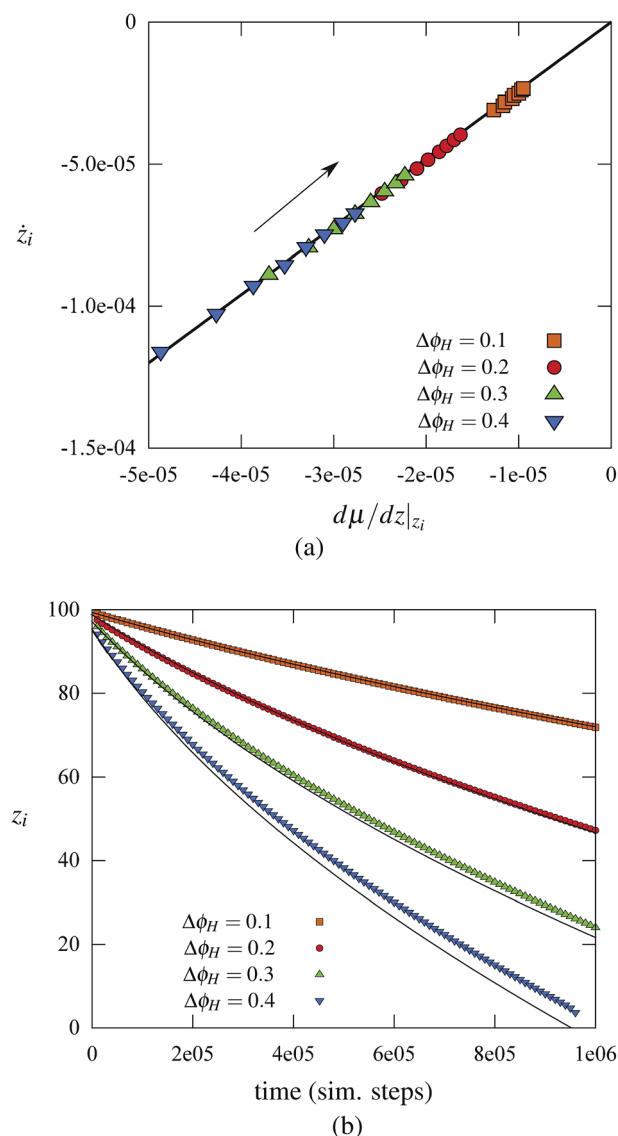


Fig. 3 Measurable quantities in the evaporation of a planar film. (a) Rate of evaporation as a function of the local gradient of the chemical potential. Symbols correspond to LB simulations. The thick black line is a linear fit to the data. The arrow indicates the direction of increasing time in the simulations, reflecting a slowing down of the interface. (b) Interface position as a function of time. Symbols correspond to LB simulations. The thick black curves correspond to the theoretical prediction, eqn (24).

To understand why the simulations deviate from the analytical predictions for large $\Delta\phi_H$, we note that two main mechanisms control the motion of the liquid front. On the one hand, evaporation takes place over a time scale $\tau_E = \int_{z_0}^0 dz_i/\dot{z}_i$ which gives

$$\tau_E = \frac{\Delta\phi z_0(2z_H - z_0)}{M(\mu_i - \mu_H)}. \quad (25)$$

On the other hand, the concentration imbalance $\Delta\phi_H$ is levelled by diffusion over a timescale, τ_D , which can be estimated using eqn (22) in scaling form:

$$\frac{\Delta\phi_H}{\tau_D} \sim \frac{M(\mu_i - \mu_H)}{z_H^2},$$

giving,

$$\tau_D \sim \frac{\Delta\phi_H z_H^2}{M(\mu_i - \mu_H)}. \quad (26)$$

Combining eqn (25) and (26) gives the ratio of diffusive to evaporative timescales,

$$\frac{\tau_D}{\tau_E} \sim \frac{\Delta\phi_H}{\Delta\phi} \left[\frac{z_0}{z_H} \left(2 - \frac{z_0}{z_H} \right) \right]^{-1}. \quad (27)$$

To verify this prediction, we measured the total evaporation time for freely evaporating films at different values of ϕ_H , z_0 and z_H . To measure the corresponding timescales for diffusive transport, we ran simulations of initially homogeneous systems where the initial condition was set to $\phi(z, 0) = -\phi_{eq}$, subject to the boundary condition $\phi(z_H, t) = \phi_H$. As the system evolved to equilibrium, we measured τ_D according to the criterion $\phi(z = z_w, \tau_D) - \phi_H = 0.9\Delta\phi_H$. Fig. 4 shows a plot of the measured τ_D/τ_E ratios as a function of $\Delta\phi_H$ where the x-axis has been normalised by the size-dependent factor in eqn (27). The evaporation time shows a strong increase as the driving chemical potential, or equivalently $\Delta\phi_H$, vanishes. The diffusion time, however, increases as $\Delta\phi_H \rightarrow 0$ at a much smaller rate: this is because while the driving chemical force vanishes at small $\Delta\phi_H$, the concentration difference to be balanced also vanishes. The ratio of both timescales grows linearly with the concentration

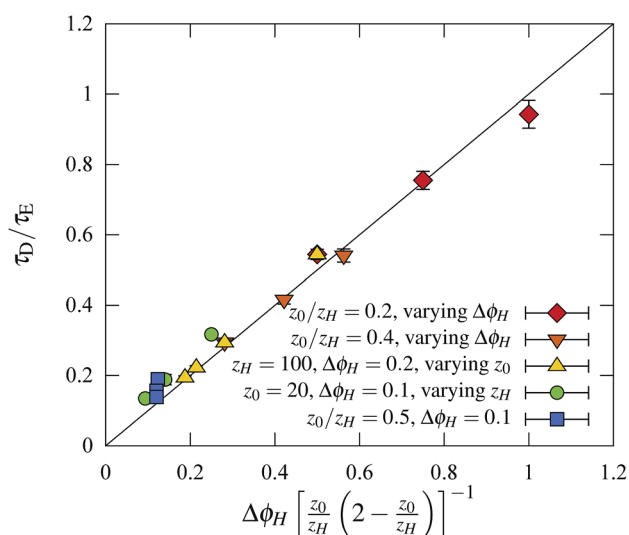


Fig. 4 Ratio of diffusive to evaporative times of planar films for different values of the driving order parameter imbalance, $\Delta\phi_H$, and the film to system size ratio, z_0/z_H . The data collapse onto a master curve as predicted by eqn (27).

difference in agreement with eqn (27). Thus the assumption of a diffusion time that is short compared to the evaporation time used to derive eqn (24) breaks down as $\Delta\phi_H$ becomes larger; this explains the increasing discrepancy between the analytical prediction and the simulation results observed in Fig. 3b for $\Delta\phi_H > 0.2$.

For water droplets evaporating at ambient temperature, the driving concentration difference of water molecules in air is much smaller than the density of the liquid. As a consequence, the ratio τ_D/τ_E is very small (of order 10^{-5}). While τ_D/τ_E is significantly larger in our simulations, there is still a sufficient separation of timescales to reproduce the quasi-static theory precisely (e.g., for a ratio of 0.25 the rate of evaporation deviated from the theoretical value by less than 5%). Altogether, the quasi-static regime of the experiments and the analytical theory can be captured by the LB simulations.

4 Evaporation of a sessile droplet

We now study the evaporation of a small 3D sessile droplet (of typical size below the capillary length) in contact with a plane. Such a simple system is convenient to analyse the evaporation of droplets in the Cahn–Hilliard model before comparing with LB simulations.

4.1 Analytical results

Consider a droplet sitting on a smooth horizontal surface (see Fig. 1b). The equilibrium shape of the droplet can be controlled by choosing the contact angle θ_e , which we take for simplicity to be the neutral wetting case $\theta_e = 90^\circ$. Because of the smoothness of the surface, the contact angle $\theta(t)$ remains close to θ_e as evaporation proceeds. Furthermore, the negligible effect of gravity at sizes below the capillary length means that the shape of the droplet is completely described by the instantaneous value of the base radius $R(t)$; it follows that the droplet volume is $V = \frac{2\pi}{3}R^3$.

For quasi-static dynamics, where $\tau_D \ll \tau_E$, the chemical potential in the ambient phase satisfies Laplace's equation. Due to the symmetry of the configuration, we consider solutions that depend only on the distance from the centre of the droplet r in a spherical co-ordinate system. At the interface we impose $\mu(R) = \mu_i$. To drive the evaporation of the droplet, we impose $\phi(R_H) = \phi_H$ which leads to $\mu(R_H) = \mu_H$, where R_H is the radius of a shell of prescribed ϕ_H .

The chemical potential profile obeys

$$\mu(r) = \mu_H - (\mu_H - \mu_i) \frac{R_H - r}{R_H - R} \left(\frac{R}{r} \right), \quad (28)$$

where $r \geq R$. Using eqn (10) and integrating over the droplet surface we obtain the rate of change of the droplet volume

$$\frac{dV}{dt} = \frac{2\pi M}{\Delta\phi} \frac{(\mu_H - \mu_i)R}{1 - \frac{R}{R_H}}, \quad (29)$$

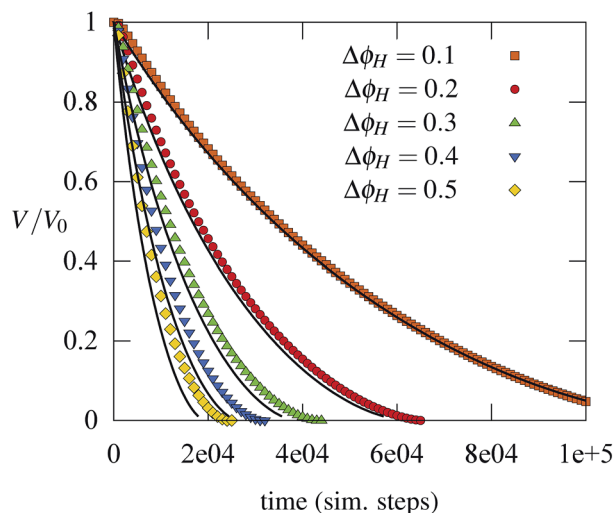


Fig. 5 Time evolution of the volume of a 3D droplet at different $\Delta\phi_H$. Symbols correspond to LB simulations. The black curves correspond to the theoretical prediction, eqn (30).

which can be integrated to give

$$\frac{3}{2} \left[V(t)^{2/3} - V_0^{2/3} \right] - \frac{V(t) - V_0}{V_H^{1/3}} = (2 \cdot 3^{1/2} \pi)^{2/3} \frac{M}{\Delta\phi} (\mu_H - \mu_i) t, \quad (30)$$

where $V_H = 2\pi R_H^3/3$. We note that eqn (30) accounts for the finite size of the system through the radius of the hemispherical shell, R_H , at which the outer boundary condition is applied. As such, this result is the analogue of results used in molecular dynamics simulations of thermal evaporation to account for a similar finite size effect.^{8,9} Crucially, in the limit of large system

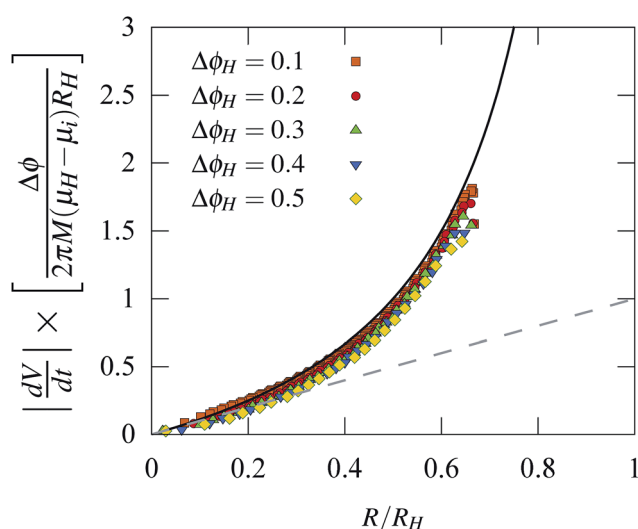


Fig. 6 Rate of evaporation as a function of the dimensionless droplet radius R/R_H for different values of ϕ_H . The data has been scaled according to eqn (29), showing a good collapse onto the master curve $(R/R_H)/(1 - R/R_H)$ (solid curve). The dashed line corresponds to the limit $dV/dt \sim R/R_H$, which is recovered for small R/R_H .

size (or small droplets), $V_0 \ll V_H$, eqn (30) reduces to the well-known 'D² evaporation law'⁸

$$R^2 \sim (t^* - t), \quad (31)$$

where t^* is the time at which the droplet vanishes completely.

4.2 LB simulations

We now test whether the LB simulations can reproduce the evaporation of 3D sessile droplets. We considered a simulation domain of dimensions $N_x \times N_y \times N_z = 100 \times 100 \times 50$.

We focus on the effect of ϕ_H on droplets of neutral wetting properties ($\theta_e = 90^\circ$). A droplet of initial radius $R_0 \approx N_z/2$ was allowed to equilibrate on top of a solid wall (located at $z_w = 1$). During the equilibration stage periodic boundary conditions were imposed at all simulation boundaries. As reported in a previous study²⁵ there is a small shrinkage of the droplets because of the competition between the bulk and surface terms in the free energy which allows mass transfer from the interface to the volume. We observe the same effect in our simulations. The change in the droplet volume was typically under 10%. After the equilibration stage we imposed the boundary condition $\phi(R_H) = \phi_H$, with $R_H = N_x/2$, to drive the evaporation of the droplet. Fig. 5 shows curves for the volume of the droplet as a function of time, along with the analytical prediction, eqn (30). We find a good agreement between theory and simulation at small $\Delta\phi_H$. As for the planar-film simulations, the agreement deteriorates for large $\Delta\phi_H$, where the relaxation of the phase field no longer occurs significantly faster than evaporation.

Beyond the results for the time evolution of the droplet size, it is instructive to plot the evaporation rate of the droplets. Fig. 6 shows the rate of change of the droplet volume as a function of R/R_H for different values of $\Delta\phi_H$. The rate of evaporation is an increasing function of R/R_H . This is because the diffusive flux increases when the surface of the droplet is in close proximity to the boundary shell. The linear regime, corresponding to the evaporation becoming independent of the size of the shell, is recovered for $R/R_H \leq 0.2$. Overall, there is a good agreement between simulations and the theoretical prediction, eqn (30), with only small deviations at the largest $\Delta\phi_H$ values considered.

5 Evaporation from a chemically patterned substrate

To illustrate the applicability of the LB method to more complex situations, we carried out simulations of a sessile droplet evaporating on a flat chemically patterned surface. Our aim is to offer a qualitative comparison between our results and experimental results presented previously.²⁶ We consider a solid surface patterned with concentric rings in which the equilibrium contact angle alternates between $\theta_e = 90^\circ$ and $\theta_e = 50^\circ$. In the simulations, this variable contact angle is implemented by imposing eqn (3) close to the contact line. The width of the rings, is $\Delta \approx 10\varepsilon$ and so is larger than the typical interface width, ε .

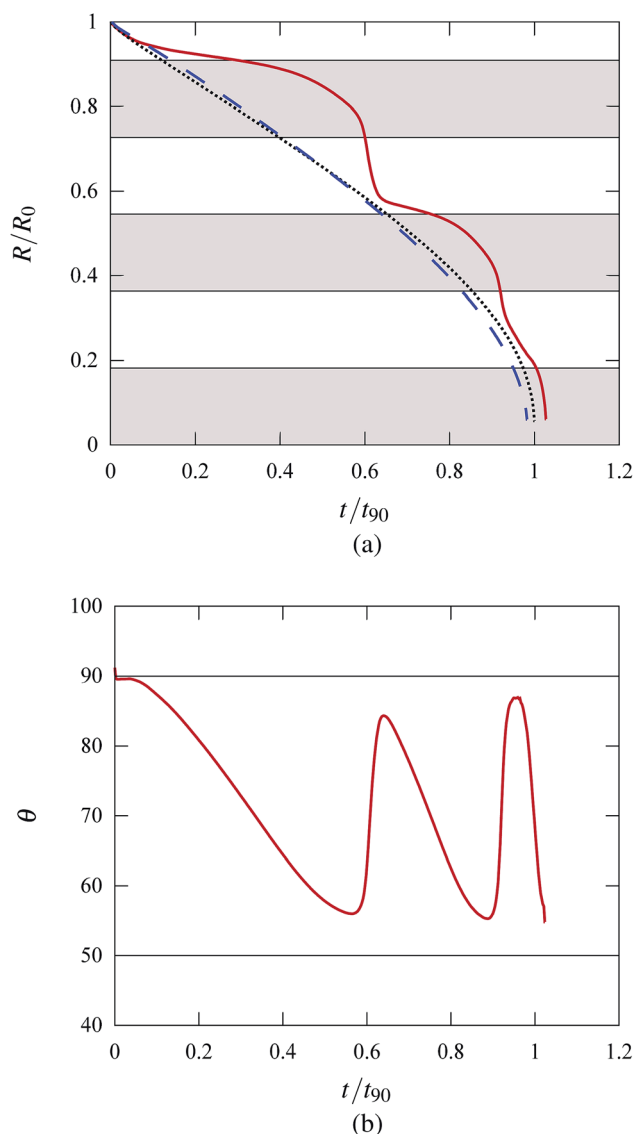


Fig. 7 Time evolution for the contact radius (a) and contact angle (b) of a sessile droplet evaporating on a chemically patterned surface. Time is measured in units of t_{90} , the evaporation time of a drop on a homogeneous surface of $\theta_e = 90^\circ$. In (a) the greyed regions correspond to $\theta_e = 50^\circ$, while white regions correspond to $\theta_e = 90^\circ$. In (b) the horizontal lines show the equilibrium contact angles of the rings.

The time evolution of the drop is characterised by measuring the instantaneous contact radius, R , and contact angle, θ . Fig. 7a shows the radius as a function of time. The dynamics of the droplet on the chemically patterned surface (red continuous curve) is composed of a series of steps consistent with the experimentally reported stick-slip dynamics. For each step the contact line initially advances freely on rings with $\theta_e = 90^\circ$, but slows down significantly as the contact line enters a ring with $\theta_e = 50^\circ$. Subsequently, as the drop enters the next hydrophobic ring, the contact line speeds up. Apart from the qualitative agreement with the experiments presented in ref. 26, our results show that the total evaporation time on the patterned surface exceeds the

evaporation time of drops of equal initial volume on homogeneous surfaces with contact angles $\theta_e = 50^\circ$ and $\theta_e = 90^\circ$ (dotted and dashed curves in Fig. 7a), in qualitative agreement with recently reported analytical results.²

Fig. 7b shows the instantaneous value of the contact angle as a function of time. Because of the finite size of the interface, the contact angle varies smoothly in time between the two equilibrium values.

Finally, in Fig. 8 we present images of the flow field during the evaporation process. The arrows show the direction of the velocity field at each point. At early times (left panel), the contact line is initially over a hydrophobic ring. The flow is directed from the top of the droplet towards the contact line. This feature is preserved as the contact line crosses to a hydrophilic ring, as shown in the middle panel and is consistent with previous theoretical results for droplets evaporating at constant contact area²⁷ (pinned contact line). Finally, the drop enters a hydrophobic ring again, and the drop shape relaxes to a higher contact angle. As a consequence, the flow pattern is reversed, with liquid flowing from the contact line to the top of the drop (also leading to a transient increase in drop height).

6 Discussion and conclusions

We have tested the validity of the lattice-Boltzmann algorithm as a way to study evaporation by comparing numerical results to analytic solutions in one and three dimensions. We showed that it is possible to achieve a ratio of diffusion to evaporation time scales, τ_D/τ_E , of between 0.1 and 1 with feasible computational resources. Although, the physical value is much smaller for the evaporation of a water droplet into air, $\tau_D/\tau_E = 0.1$ was found to give a sufficient separation of timescales to allow an excellent match between the simulations and the exact results (obtained in the limit $\tau_D/\tau_E = 0$). It would also be interesting to use the algorithm to investigate systems for which the diffusive and evaporative timescales are not sharply separated, $\tau_D/\tau_E \sim 1$. For example, colloidal liquid pairs are increasingly used in microfluidics to mimic nanometric systems due to their ultra-low surface tension and large interface thickness.^{13,14} These systems often have comparable densities and solubilities which can lead to timescale ratios of order unity.

In the 3D case we introduced 'shell' boundary conditions which allow an exact solution for a finite geometry. On the other hand, it is also possible to simulate freely evaporating droplets, as finite size effects droplet below 5% when the ratio of the radii of droplet and boundary is less than ≈ 0.2 .

The lattice-Boltzmann approach used here does not take heat transport into account. Our model is therefore valid for situations where any excess latent heat can be quickly removed by, for example, thermal coupling to the substrate. Here we use the phase field ϕ to label the different phases, and density is constant. This does not affect the evaporation process, but care must be taken about dissipation and inertia in the gas phase in dynamical simulations.

To illustrate the applicability of our LB approach in more complex situations, we have carried out simulations of a droplet evaporating on a chemically patterned surface. Our results show

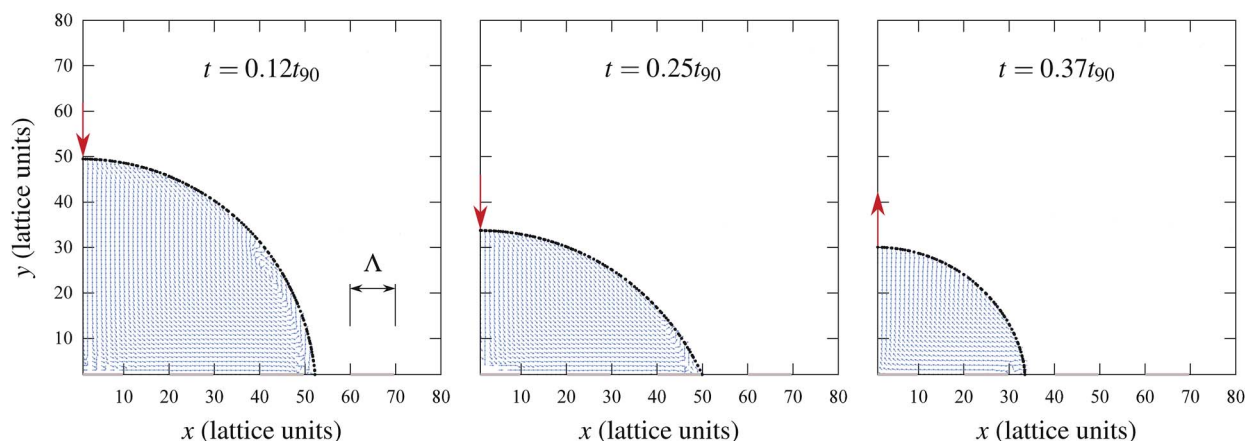


Fig. 8 Flow field at different times within a sessile droplet evaporating on a chemically patterned surface. The surface is composed of concentric rings of varying contact angle: $\theta_e = 90^\circ$ (black portions of x axis) and $\theta_e = 50^\circ$ (light grey portions of x axis). The light red arrows show the direction of motion of the top of the drop at a given time.

good qualitative agreement with previous studies, further supporting the validity of LB to study evaporation phenomena subject to complex boundary conditions. We hope that the availability of the lattice-Boltzmann algorithm as a tool to model evaporation (and, equally condensation) will motivate further work to examine more complex situations focusing on the interplay between the fluid dynamics, capillarity and evaporation. These might include the change in evaporation rates due to moving air currents and the dynamics of droplets and fronts in complex geometries.

Acknowledgements

This publication is based on work supported in part by Award no. KUK-C1-013-04, made by King Abdullah University of Science and Technology (KAUST) (RL-A and DV) and by the ERC Advanced Grant (MiCE) (JMY).

References

- 1 A. Cazabat and G. Guena, *Soft Matter*, 2010, **6**, 2591–2612.
- 2 J. M. Stauber, S. K. Wilson, B. R. Duffy and K. Sefiane, *J. Fluid Mech.*, 2014, **744**, 1–12.
- 3 M. Faustini, C. Boissiere, L. Nicole and D. Grosso, *Chem. Mater.*, 2014, **26**, 709–723.
- 4 B. Roman and J. Bico, *J. Phys.: Condens. Matter*, 2010, **22**, 493101.
- 5 C. Py, P. Reverdy, L. Doppler, J. Bico, B. Roman and C. N. Baroud, *Phys. Rev. Lett.*, 2007, **98**, 156103.
- 6 T. Tanaka, M. Morigami and N. Atoda, *Jpn. J. Appl. Phys.*, 1993, **32**, 6059.
- 7 K. Singh, J. R. Lister and D. Vella, *J. Fluid Mech.*, 2014, **745**, 621–646.
- 8 R. Holyst, M. Litniewski, D. Jakubczyk, K. Kolwas, M. Kolwas, K. Kowalski, S. Migacz, S. Palesa and M. Zientara, *Rep. Prog. Phys.*, 2013, **76**, 034601.
- 9 R. Holyst and M. Litniewski, *Phys. Rev. Lett.*, 2008, **100**, 055701.
- 10 S. Chen and G. Doolen, *Annu. Rev. Fluid Mech.*, 1998, **30**, 329–364.
- 11 H. Kusumaatmaja, M. L. Blow, A. Dupuis and J. M. Yeomans, *Europhys. Lett.*, 2008, **81**, 36003.
- 12 K. Connington and T. Lee, *J. Comput. Phys.*, 2013, **250**, 601–615.
- 13 S. A. Setu, I. Zacharoudiou, G. J. Davies, D. Bartolo, S. Moulinet, A. A. Louis, J. M. Yeomans and D. G. A. L. Aarts, *Soft Matter*, 2013, **9**, 10599–10605.
- 14 R. Ledesma-Aguilar, I. Pagonabarraga and A. Hernández-Machado, *Phys. Fluids*, 2007, **19**, 102113.
- 15 B. M. Mognetti, H. Kusumaatmaja and J. M. Yeomans, *Faraday Discuss.*, 2010, **146**, 153–165.
- 16 M. Sbragaglia, K. Sugiyama and L. Biferale, *J. Fluid Mech.*, 2008, **614**, 471–493.
- 17 H. Safari, M. H. Rahimian and M. Krafczyk, *Phys. Rev. E: Stat., Nonlinear, Soft Matter Phys.*, 2013, **88**, 013304.
- 18 A. Bray, *Adv. Phys.*, 1994, **43**, 357–459.
- 19 E. B. Dussan, *Annu. Rev. Fluid Mech.*, 1979, **11**, 371–400.
- 20 A. J. Briant and J. M. Yeomans, *Phys. Rev. E: Stat., Nonlinear, Soft Matter Phys.*, 2004, **69**, 031603.
- 21 D. Sibley, A. Nold, N. Savva and S. Kalliadasis, *Eur. Phys. J. E*, 2013, **36**, 26.
- 22 J.-C. Desplat, I. Pagonabarraga and P. Bladon, *Comput. Phys. Commun.*, 2001, **134**, 273–290.
- 23 A. Ladd and R. Verberg, *J. Stat. Phys.*, 2001, **104**, 1191–1251.
- 24 C. M. Pooley and K. Furtado, *Phys. Rev. E: Stat., Nonlinear, Soft Matter Phys.*, 2008, **77**, 046702.
- 25 P. Yue, C. Zhou and J. J. Feng, *J. Comput. Phys.*, 2007, **223**, 1–9.
- 26 N. Anantharaju, M. Panchagnula and S. Neti, *J. Colloid Interface Sci.*, 2009, **337**, 176–182.
- 27 H. Gelderblom, O. Bloemen and J. H. Snoeijer, *J. Fluid Mech.*, 2012, **709**, 69–84.